Full Length Article

Synthesis of hierarchical ZnV_2O_6 nanosheets with enhanced activity and stability for visible light driven CO_2 reduction to solar fuels

Abdullah Bafaqeer, Muhammad Tahir*, Nor Aishah Saidina Amin

Chemical Reaction Engineering Group (GREG), Faculty of Chemical and Energy Engineering, Universiti Teknologi Malaysia, UTM, Johor Bahru, Johor, 81310, Malaysia

A B S T R A C T

Hierarchical nanostructures have lately garnered enormous attention because of their remarkable performances in energy storage and catalysis applications. In this study, novel hierarchical ZnV_2O_6 nanosheets, formulated by one-step solvothermal method, for enhanced photocatalytic CO_2 reduction with H_2O to solar fuels has been investigated. The structure and properties of the catalysts were characterized by XRD, FESEM, TEM, BET, UV–vis, Raman and PL spectroscopy. The hierarchical ZnV_2O_6 nanosheets show excellent performance towards photoreduction of CO_2 with H_2O to CH_3OH, CH_3COOH and HCOOH under visible light. The main product yield, CH_3OH of 3253.84 µmol g-cat^{-1} was obtained over ZnV_2O_6, 3.4 times the amount of CH_3OH produced over the ZnO/V_2O_5 composite (945.28 µmol g-cat^{-1}). In addition, CH_3OH selectivity of 39.96% achieved over ZnO/V_2O_5, increased to 48.78% in ZnV_2O_6 nanosheets. This significant improvement in photo-activity over ZnV_2O_6 structure was due to hierarchical structure with enhanced charge separation by V_2O_5. The obtained ZnV_2O_6 hierarchical nanosheets exhibited excellent photocatalytic stability for selective CH_3OH production.

© 2017 Elsevier B.V. All rights reserved.

1. Introduction

Photocatalytic reduction of CO_2 to useful chemicals and fuels has grown an intense area of research owing to global warming and energy crises. During the last years, artificial photosynthesis process to convert CO_2 into useful carbon sources such as CO, HCOOH, HCHO, CH_3OH and CH_4 has been attractive alternatives because of the demand for methods to recycle CO_2 as a natural resource [1–3]. The solar photocatalytic conversion of CO_2 into value added fuels or chemical products is one of the most attractive strategies [4,5]. Thus, many research efforts have been made to develop efficient photocatalysts for the reduction of CO_2 such as $InNbO_4$ [6], $g-C_3N_4$ [7], $CaFe_2O_4$ [8], TiO_2 [9–11], ZnO [12–14], $NaBiO_3$ [15]. Among all, ZnO has been a widely studied semiconductor because of its strong oxidation and reduction abilities [16–18]. In addition, it is environmentally friendly, relatively cheap and can be grown in various nanostructures via cost effective methods [19,20]. However, because of wide band gap energy (∼3.2 eV), ZnO can only be activated under UV light irradiation. Furthermore, it has high charges recombination rate, resulted in poor photocatalytic performance. So, it is imperative to expand the absorption

band of ZnO towards visible region of solar spectrum. To address these problems, many approaches have been made such as preparing quantized ZnO nanocrystallites [21], depositing noble metals [22,23], surface photo-sensitization [24] and forming carbon-based composites [25–27].

One of the main approaches to improve ZnO activity under visible light is coupling with low band gap energy semiconductors which can extend optical absorption towards visible part of the solar spectrum. In this perspective, vanadium pentoxide (V_2O_5), an important transition metal oxide with a typical narrow band gap (∼2.3 eV) can be a good candidate for capturing visible light [28,29]. Coupling V_2O_5 with ZnO could be efficient to enhanced photoactivity under visible light. Both zinc and vanadium are earth abundant, relatively economical, and can offer several oxidation states, which can render a broad range of redox reactions [30].

Recently, hierarchical nanostructures such as nanosheets, nanorods, or nanoplates have garnered enormous attention in energy storage, photochemical and other applications [31,32]. Therefore, developing zinc-vanadium nanostructures could enhance both photoactivity and selectivity compared to ZnO/V_2O_5 composite. In this perspective, ZnV_2O_4 has gained attention because of its interesting structural changes at low temperatures [33]. Different nanostructures of ZnV_2O_4 have been reported like hollow spheres, clewlike hollow structures, nanosheets, and glomerulus nano/microspheres for various applications [33–36].

The ZnV_2O_4 hollow spheres shows a good adsorption capacity of methylene blue (MB) organic pollutant. Likewise, clewlike hollow ZnV_2O_4 spheres have been synthesized by the reaction between zinc nitrate hexahydrate and ammonium metavanadate in benzyl alcohol [34]. ZnV_2O_4 spinel oxide nanosheets were prepared in oxalic acid dehydrated using zinc acetate and ammonium meta-vanadate as the raw materials [35]. The ZnV_2O_4 nanosheets are a prospective material for hydrogen energy storage have shown good charge-discharge performance in lithium ion batteries and as a promising photocatalyst. However, structured ZnV_xO_y based photo-catalyst has never been reported for CO_2 reduction application. Therefore, it is appropriate to explore hierarchical ZnV_2O_6 semiconductors for photocatalytic CO_2 reduction applications under solar energy.

Herein, we successfully designed and synthesized novel 2D ZnV_2O_6 nanosheets through a single-step solvothermal process. The materials were investigated for photocatalytic CO_2 reduction by H_2O to fuels under visible light irradiations. The ZnV_2O_6 nanosheets showed enhanced photocatalytic activity for converting CO_2 to CH_3OH, $HCOOH$ and CH_3COOH. The structured ZnV_2O_6 nanosheets found very efficient for selective methanol production compared to ZnO/V_2O_5 composite. The remarkably enhanced photocatalytic performance was ascribed to the exceptional hierarchical structure associated with ZnV_2O_6. The effect of the contents of catalysts on photocatalytic activity and the stability of ZnV_2O_6 nanosheets were investigated systematically.

2. Experimental

2.1. Preparation of novel ZnV_2O_6 catalyst

The ZnV_2O_6 nanosheets were prepared using a solvothermal method. Typically, 2.052 mmol of ammonium metavanadate [NH_4VO_3] was added into 20 ml of N,N-dimethyl formamide (DMF). After stirring for 10 min, zinc acetate [$Zn(O_2CCH_3)_2$] was added to above solution under continuous stirring to obtain a homogenous solution. Oxalic acid dehydrated [$H_2C_2O_4\cdot2H_2O$] was added afterward. The ratio of oxalic acid to NH_4VO_3 was adjusted to 1:3. After being stirred for 30 min, the obtained solution was transferred into a 75 ml Teflon lined autoclave, which was maintained at 200 °C for 24 h and then cooled to room temperature. The black colour precipitates collected were washed several times with absolute ethanol and DI water. Finally, the products were dried in air flow oven at 80 °C for 12 h. The as prepared ZnV_2O_6 were calcined at 550 °C for 3 h and efficiency between as prepared and calcined materials was compared. The ZnV_2O_6 samples were prepared at different heating times of 12 h, 48 h and 72 h using the same procedure.

2.2. Materials characterization

The crystalline structure was determined using X-ray diffractometer (Rigaku Smart Lab) with Cu-Kα radiation (λ = 0.154178 nm) operated at 40 kV and 30 mA. The XRD patterns were obtained with a scanning rate of 0.02° min^{-1} and scanning range of 3–100° of 2θ. The morphology of the samples was examined by field emission scanning electron microscopy (FE-SEM, ZEISS Crossbean 340). The high-resolution transmission electron microscope (HR-TEM) images of the modified nanoparticles were obtained in a transmission electron microscope (TEM, HITACHI HT7700). Nitrogen-adsorption-desorption isotherms were collected using Micromeritics ASAP 2020 at 77 K, after degassing the samples at 523 K for 4 h under vacuum and using the nitrogen flux. The BET surface area and pore diameter were calculated from the desorption branch of isotherms according to BJH method. Ultraviolet–visible (UV–vis) diffuse reflectance absorbance spectra were carried out on a Cary 100 Agilent UV–vis spectrophotometer (Model G9821A) equipped with an integrated sphere in the wavelength range of 200–800 nm. Raman and photoluminescence (PL) spectra of samples were recorded at room temperature using Raman Spectrometer (LabRAM HR Evolution, HORIBA), whereas PL was conducted using a laser of 325 nm and RAMAN with a laser of 532 nm as excitation source.

2.3. Photocatalytic activity

The schematic presentation of the slurry type photoreactor for CO_2 reduction is illustrated in Fig. 1. The CO_2 reduction reaction was performed using a quartz glass with a volume of 150 m. A 35W HID Xe lamp was used as a visible light source with a light intensity of 20 MW cm^{-2} measured using a reference solar cell (91150 V, Newport) [37]. First, 100 mg photo-catalyst was suspended in 100 ml distilled water containing 0.1 M NaOH solution under magnetic stirring. Then, compressed CO_2 gas regulated by mas flow controller was continuously bubbled through the solution for 30 min to remove the oxygen before starting experiment. The temperature of the reactor was controlled by circulating cooled water. The control experiments were conducted at 25 °C, 1 atm and feed flow rate 20 ml/min. The lamp was turned on to start the photoreaction under continuous CO_2 flow rate. During the reaction process, the liquid products were taken out after 2 h intervals, then were centrifuged using Syringe Filter with Nylon Membrane, pore size 0.45 μm and diameter 33 mm to remove catalysts. The concentration of methanol, formic acid and acetic acid were analyzed by a gas chromatograph (GC-7820A) equipped with a flame ionization detector (FID) and HP-5 capillary column. Control experiments were carried out in the dark or without catalyst under the same experimental conditions. The calibration of the GC was conducted using standard solutions of methanol, formic acid and acetic acid. More importantly, methanol peaks areas obtained were consistent in multiple injections, yet peak areas obtained for formic acid and acetic acid were different in different injections and their average values have been used for calibration curve. This was perhaps due to FID detector was not well-suited for the analysis of formic acid and acetic acid.

3. Results and discussion

3.1. Morphology of catalysts

Fig. 2(a) shows XRD patterns of the bare and calcined ZnV_2O_6 nanosheets samples. Clearly, the XRD pattern of the bare ZnV_2O_6 shows one pronounced diffraction peak located at around 2θ = 10.0°. Such a diffraction pattern can be attributed to the ZnV_2O_6 phase, which is a characteristic of metal alkoxides [38,39]. As expected, the bare ZnV_2O_6 can be converted into highly crystalline ZnV_2O_6 nanosheets after calcining at 550 °C for 3 h in air atmosphere. All the identified diffraction peaks can be assigned to ZnV_2O_6 with an orthorhombic structure (JCPDS Card No. 01-074-1262). In addition, weak diffraction peaks of V_2O_5 appeared, indicating the presence of small amounts of V_2O_5 (JCPDS Card No. 01-072-0433) and the resulting sample was a mixture of ZnV_2O_6 and V_2O_5. Fig. 2(b) shows the interesting crystal geometry of spinel oxide ZnV_2O_6, which is formed by ZnO_4 tetrahedra and VO_6 octahedra. It belongs to the FCC type crystal structure with Fd3m symmetry group. According to crystallographic studies, zinc atoms reside in the tetrahedral 8a position whereas the vanadium atoms are on 16d position, which forms a network of corner sharing tetrahedral structure. The oxygen ions are located at the 48e position [31].
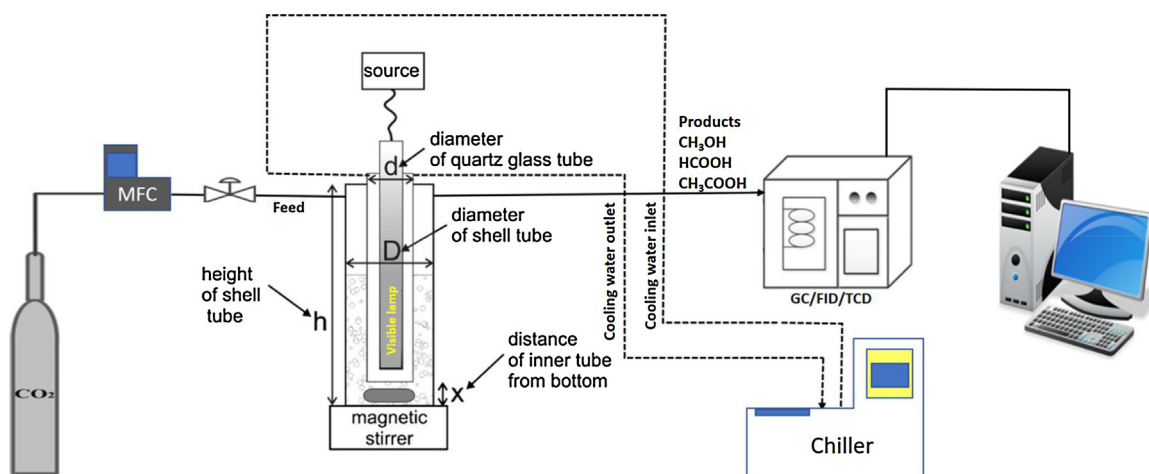
Fig. 1. Schematic of experimental set up for photoreaction of CO_2 with H_2O under visible light.
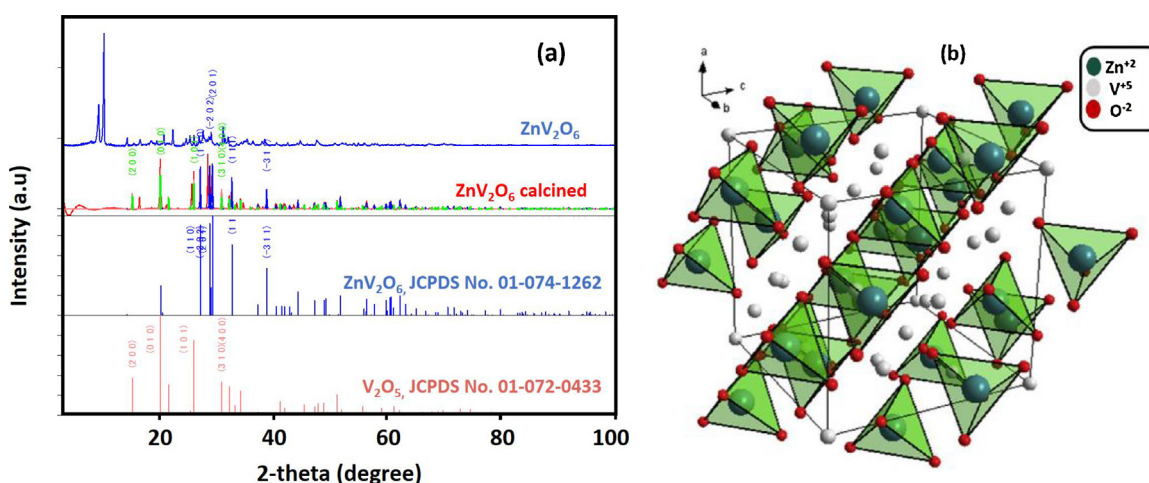

Fig. 2. (a) XRD pattern of ZnV_2O_6 and ZnV_2O_6 calcined nanosheets; (b) Crystal structure of spinel ZnV_2O_6 with corresponding atoms (green, white and red spheres represent zinc, vanadium and oxygen atoms, respectively). (For interpretation of the references to colour in this figure legend, the reader is referred to the web version of this article.)

Table 1
Summary of physiochemical characteristics of ZnV_2O_6 sample.

Sample	BET surface area S_{BET} (m^2/g)	BJH surface area S_{BJH} (m^2/g)	Pore volume (cm^3/g)	Pore width (nm)	Crystal size d_{xrd} (nm)	Band gap (E_{bg})
ZnV_2O_6	11.57	3.80	0.0045	17.3	1.355	2.02

The surface area (S_{BET}), pore volume and pore size of ZnV_2O_6 sample is reported in Table 1. The BET surface area of ZnV_2O_6 was 11.57 m^2/g and the BJH surface area of 3.8 m^2/g. Previously, BET surface of ZnV_2O_4 of 6.1 m^2/g has been reported [40]. This revealed a higher BET surface area of ZnV_2O_6 compared to ZnV_2O_4 sample due to their different hierarchical structures. Similarly, the pore volume and pore diameter of 0.0045 cm^3/g and 17.3 nm for ZnV_2O_6 sample were obtained, respectively. The reduced pore diameter was possibly due to the controlled crystal growth in the ZnV_2O_6 sample via one-step solvothermal method. Therefore, well-developed ZnV_2O_6 structure with larger BET surface area and smaller pore diameter could minimize mass transfer limitations to increase catalyst activity.

The morphology and microstructural features of the ZnV_2O_6 nanosheets were investigated by field emission scanning electron micrographs (FESEM) and transmission electron microscopy (TEM). Fig. 3 shows the FESEM and TEM images of the samples obtained at different reaction stages. It can be seen in Fig. 3(a)

that the ZnV_2O_6 sample prepared at 12 h reaction time composed of intermediate products which consists of many compact sheets. However, when the reaction time was increased to 24 h, large amounts of sheets were formed as shown in Fig. 3(b). Evidently, pure ZnV_2O_6 has hierarchical microstructure consisting of uniform size nanosheets. Moreover, when the ZnV_2O_6 nanosheets prepared after 24 h reaction time were calcined at 550 °C for 3 h, they were partially disordered with improved surface roughness and reduced in size as shown in Fig. 3(c). This revealed that calcination temperature has an impact on the structure and morphology of ZnV_2O_6 nanosheets. The TEM images of bare ZnV_2O_6 sample prepared after 24 h reaction time is presented in Fig. 3(d–f). Fig. 3(d) shows ZnV_2O_6 hierarchical microstructure composed of many compact smaller nanosheets. The interplaner distance was found to be 0.48 nm and 0.42 nm, which corresponds to (111) and (101) planes of ZnV_2O_6 and V_2O_5, respectively as shown in Fig. 3(e) [31,41]. The SAED pattern of ZnV_2O_6 in Fig. 3(f) shows an obvious polycrystalline ring due to the good crystallization of ZnV_2O_6.
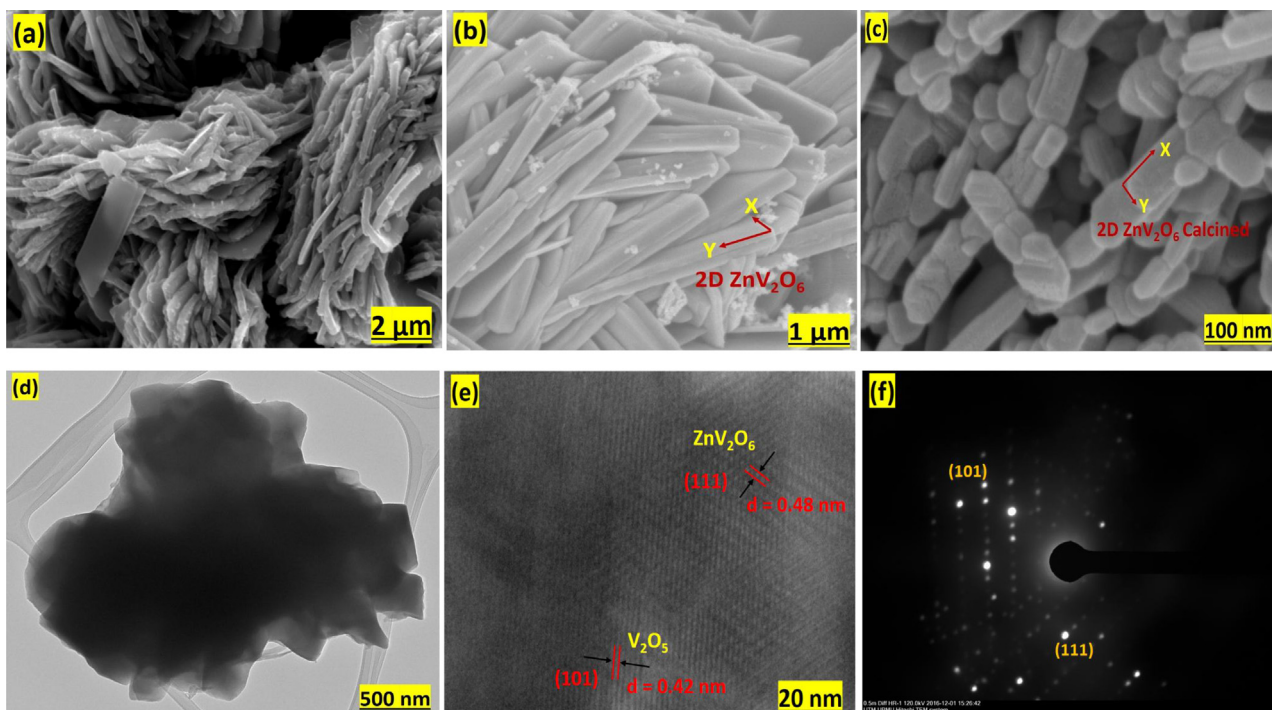
Fig. 3. Morphologies of 2D ZnV_2O_6 sample prepared at 200 °C for different reaction times: (a) SEM image of ZnV_2O_6 after 12 h, (b) SEM image of ZnV_2O_6 after 24 h, (c) SEM image of calcined ZnV_2O_6 after 24 h, (d) TEM image of ZnV_2O_6 after 24 h, (e) HR-TEM image of lattice fringes of ZnV_2O_6 sample, (f) SAED pattern of the ZnV_2O_6 sample.
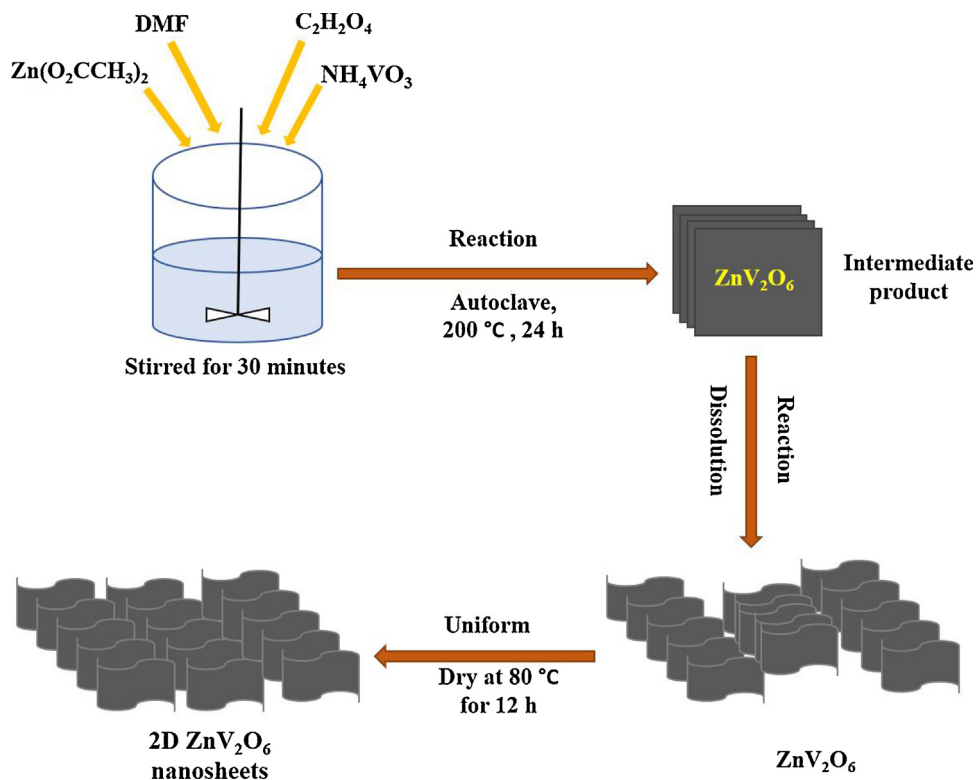

Fig. 4. Schematic illustration for the formation process of 2D ZnV_2O_6 nanosheets.

The schematic of growth mechanism for hierarchical 2D ZnV_2O_6 nanosheets is portrayed in Fig. 4. Initially, sheet intermediate product with compact nanosheets was formed in large quantity which might provide the reaction sites and sources for the impending next step [36]. Rising the reaction time, abundant ZnV_2O_6 sheet were generated by in situ reduction and continuous dissolution of the sheets intermediate product, and simultaneously aggregated into nanosheets to reduce surface energy. As the reaction proceeded in longer time, the nanosheets completely aggregated to regular nanosheets with relatively smooth surface and 2D structure.

Fig. 5 shows UV–vis diffuse reflectance absorbance spectra of the ZnO/V_2O_5 composite, bare ZnV_2O_6 and ZnV_2O_6 calcined

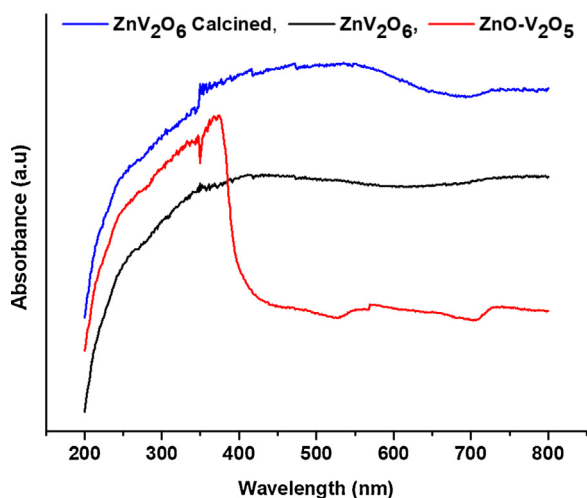**Fig. 5.** UV–vis absorbance spectra of ZnO/V$_2$O$_5$ composite, ZnV$_2$O$_6$ nanosheets and calcined ZnV$_2$O$_6$ nanosheets.

nanosheets. The combining V$_2$O$_5$ with ZnO shifted band gap energy towards visible light region. The energy band gaps (E$_{bg}$) of all the samples were obtained from the extrapolation of Tauc plot to the abscissa of photon energy (eV). The wavelengths of the ZnO/V$_2$O$_5$, ZnV$_2$O$_6$ and ZnV$_2$O$_6$ calcined samples are 447 nm, 613 nm and 685 nm corresponding to the band gap energy of 2.77 eV, 2.02 eV, and 1.81 eV, respectively. Obviously, ZnV$_2$O$_6$ nanosheets displays higher absorption intensities than ZnO/V$_2$O$_5$ composite in the visible light region. Calcining ZnV$_2$O$_6$ nanosheets further shifted absorbance of ZnV$_2$O$_6$ towards higher wavelength of visible light irradiations.

Raman spectra of the pure ZnV$_2$O$_6$ and ZnO/V$_2$O$_5$ samples are depicted in Fig. 6(a). The peaks in the range of 100–1100 cm^{-1} are observed in the pure ZnV$_2$O$_6$ and ZnO/V$_2$O$_5$ samples. The characteristic peaks of ZnV$_2$O$_6$ at 81, 276, 502, 698 and 900 cm^{-1} and the peaks of ZnO/V$_2$O$_5$ at 208, 311, 423 and 742 cm^{-1} are observed in the Raman spectrum. However, the changes are obvious in the position and width of the ZnV$_2$O$_6$ sample peaks. With using one-step solvothermal method, the width of the Raman bands, in particular the peaks increased and the position is slightly shifted toward higher wavenumber, attributed to the reduction of particle size of the ZnV$_2$O$_6$ samples with higher mobility of charges.

Fig. 6(b) shows PL emission spectra of the pure ZnV$_2$O$_6$, ZnV$_2$O$_6$ calcined and ZnO/V$_2$O$_5$ samples excited at a wavelength of 325 nm. ZnO/V$_2$O$_5$ sample displays a broad PL emission peak at 380 and 510 nm that are composed of emissions due to band gap excitations, the interstitial Zn atoms and the excitations between Zn and singly charges surface oxygen, respectively [42]. These bands, in the order of their appearance are marked as "a" and "b" in Fig. 6(b). The ZnV$_2$O$_6$ nanosheets show lower PL emission intensity compared with the ZnV$_2$O$_6$ calcined and ZnO/V$_2$O$_5$. The weaker intensity of the peak represents the lower recombination probability of free charges, which indicates that coupling of vanadium with ZnO to ternary ZnV$_2$O$_6$ structure using one-step solvothermal method can effectively mitigate the recombination of photo-generated electron hole pairs. The ZnV$_2$O$_6$ calcined displays higher PL emission intensity compared with the ZnV$_2$O$_6$ nanosheets due to different phase structure and morphology as evidenced by XRD and FESEM analysis.

3.2. Photocatalytic CO$_2$ reduction with H$_2$O

The control experiments were conducted for CO$_2$ reduction with H$_2$O under visible light irradiation at room temperature, atmo-

spheric pressure, and feed flow rate 20 ml/min. In all cases, carbon containing products were not detected, thus, any carbon based products would be produced during CO$_2$ reduction process.

In order to study the effect of reaction medium, the performance of ternary ZnV$_2$O$_6$ nanosheets for CO$_2$ reduction was investigated using pure water and sodium hydroxide (NaOH) solution and the results are shown in Fig. 7(a). It is obvious that CO$_2$ reduction in the presence of 0.1 M NaOH registered high yield of CH$_3$OH which is 2250.5 μmol g-cat^{-1} for ternary ZnV$_2$O$_6$ nanosheets, 1.6 fold higher than using pure H$_2$O. This happens mainly because NaOH increases the dissolved CO$_2$ concentration in the medium and prevents recombination rate of the hole and electron pairs. In addition, highly concentrated OH$^-$ ions in the aqueous solution act as strong holes scavengers and forms OH radicals. This consequently leads to more utilization of surface electrons that stimulates CO$_2$ reduction to CH$_3$OH.

Fig. 7(b) displays the effect of different ZnO, V$_2$O$_5$, ZnO/V$_2$O$_5$, ZnV$_2$O$_6$ and ZnV$_2$O$_6$ calcined catalysts samples photoactivity for dynamic CO$_2$ conversion with 0.1 M NaOH solution under visible light irradiation. The effectiveness of the catalyst samples were analysed based on the yield of CH$_3$OH, HCOOH and CH$_3$COOH which were the three products from the process. Pure ZnO, V$_2$O$_5$ and ZnO/V$_2$O$_5$ nanocatalyst synthesized by the sol–gel method scarcely reduced CO$_2$ and showed very poor activity for CH$_3$OH formation. However, the production of CH$_3$OH was significantly enhanced using novel ZnV$_2$O$_6$ nanosheets due to hierarchical structure, efficient visible light absorption, efficient charge transfer property and higher electron mobility by coupling of vanadium with ZnO using one-step solvothermal method. In addition, the enhanced photocatalytic activity of ZnV$_2$O$_6$ nanosheets was attributed to electron trapping and hindered recombination rate by V$_2$O$_5$ presented in the sample as evidenced by XRD analysis [43].

More importantly, ZnV$_2$O$_6$ calcined at 550 °C for 3 h shows very poor activity under the same operating conditions. According to PL emission spectra, the calcined ZnV$_2$O$_6$ sample displays higher PL emission intensity compared with the bare ZnV$_2$O$_6$ nanosheets. Lately, Zhang et al. [39] reported similar observations while investigating hydrogen evolution from water using BiFeO$_3$, Bi$_2$Fe$_4$O$_9$ and BiFeO$_3$/Bi$_2$Fe$_4$O$_9$ heterojunction nanofibers under visible light irradiation. Therefore, lower photo-activity of calcined ZnV$_2$O$_6$ sample was probably due to reduction of ZnV$_2$O$_6$ at elevated temperature with different phase structure and much lower band gap energy (E$_{bg}$ = 1.81 eV). Additionally, calcined samples would be favourable for CO$_2$ reduction to hydrogen and other chemicals that were not detected in the product mixture. This is because production of CH$_3$OH was not much altered in calcined sample but the HCOOH and CH$_3$COOH production were significantly reduced. However, further investigations would be required to find out possible reasons in reduced ZnV$_2$O$_6$ catalyst activity after calcination.

Fig. 7(c) shows the effect of different catalyst preparation times of 12 h, 24 h, 48 h and 72 h at one fixed temperature (200 °C) for the prepared ZnV$_2$O$_6$ catalysts for CO$_2$ photo-reduction with H$_2$O under visible light irradiation. The effectiveness of the different heating times of samples were analysed based on the yield of CH$_3$OH, HCOOH and CH$_3$COOH which were the three products from the process. The result shows that the effect of exposure time of heating for 24 h for the prepared ZnV$_2$O$_6$ sample exhibits much higher photoactivity for CH$_3$OH, HCOOH and CH$_3$COOH evolution than the exposure time of heating for 12 h. However, catalyst preparation time of 48 h and 72 h have no significant effect on production rate and selectivity. Therefore, ZnV$_2$O$_6$ samples prepared at exposure time of 24 h were further used to investigate the effect of irradiation time and stability analysis.

Further investigations were carried out to study the effect of irradiation time on dynamic photocatalytic CO$_2$ reduction in a continuous photoreactor operation. The production of CH$_3$OH and
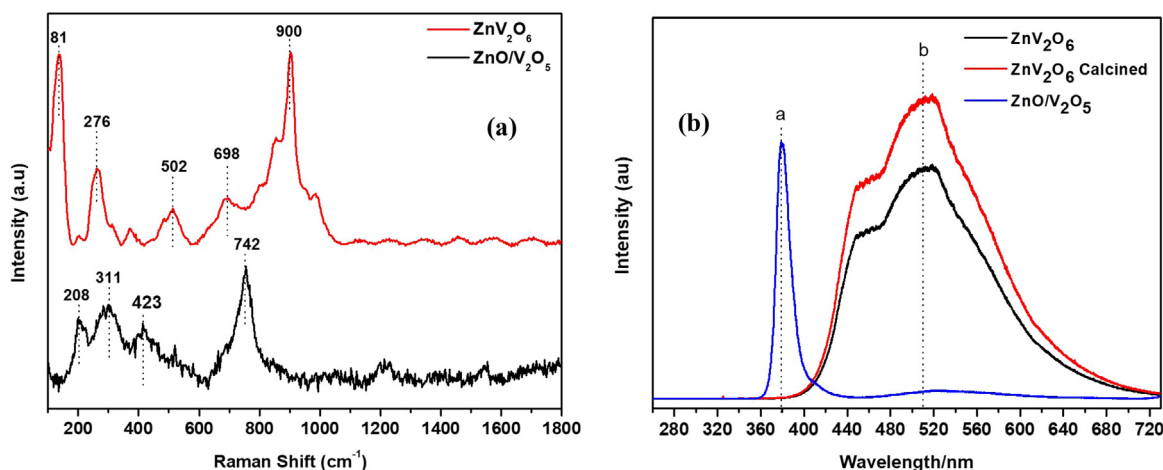
Fig. 6. (a) Raman spectra of ZnV_2O_6 nanosheets and ZnO/V_2O_5 composite; (b) Photoluminescence spectra for ZnV_2O_6 nanosheets, calcined ZnV_2O_6 and ZnO/V_2O_5 composite samples.
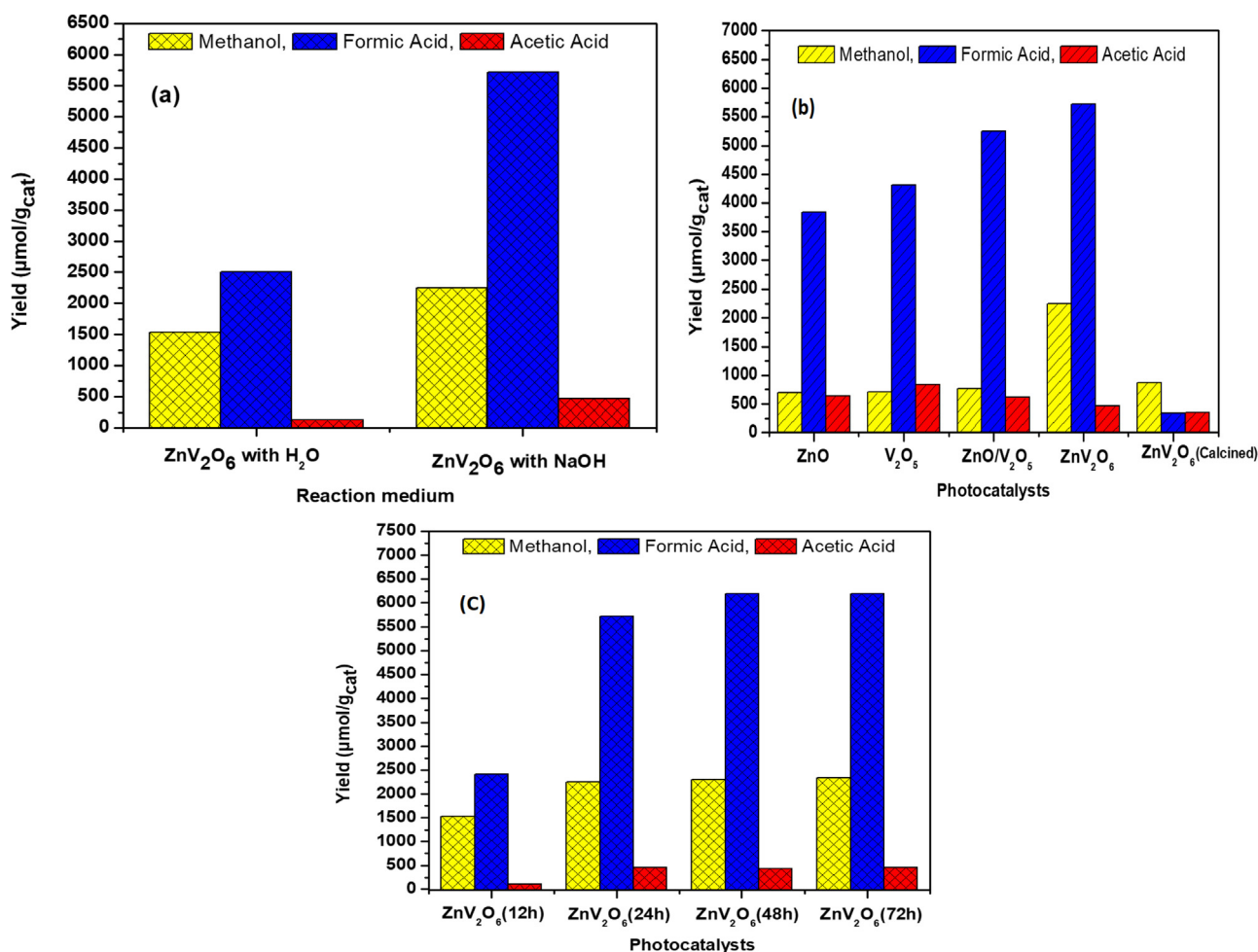

Fig. 7. (a) Yield of methanol, formic acid and acetic acid for different reaction mediums; (b) Yield of methanol, formic acid and acetic acid over various photo-catalysts; (c) Effect of different exposure times of heating for 12 h, 24 h, 48 h and 72 h for prepared ZnV_2O_6 catalyst for CO_2 photo reduction: reaction parameters (Room temperature, atmospheric pressure, feed flow rate 20 ml/min and irradiation time 2 h).

CH_3COOH gradually increased with increasing the time up to an optimum, whereas the HCOOH was decreased and then remained constant as showed in Fig. 8. Fig. 8(a) shows the yield of CH_3OH on ZnO/V_2O_5 and ZnV_2O_6 catalysts under visible light irradiation. It can be seen that ZnO/V_2O_5 has a lower photoactivity towards CH_3OH generation in the photocatalytic reduction of CO_2 com-pare with ZnV_2O_6. After irradiation time of 10 h, the CH_3OH yield of 3253.84 μmol g-cat^{-1} over ZnV_2O_6 was obtained, 3.4 times higher than that of ZnO/V_2O_5 (945.28 μmol g-cat^{-1}). This revealed that solvothermal method has a positive impact on the photocat-alytic performance of ternary ZnV_2O_6 nanosheets comparing to the ZnO/V_2O_5 composite prepared by sol-gel method. Therefore,

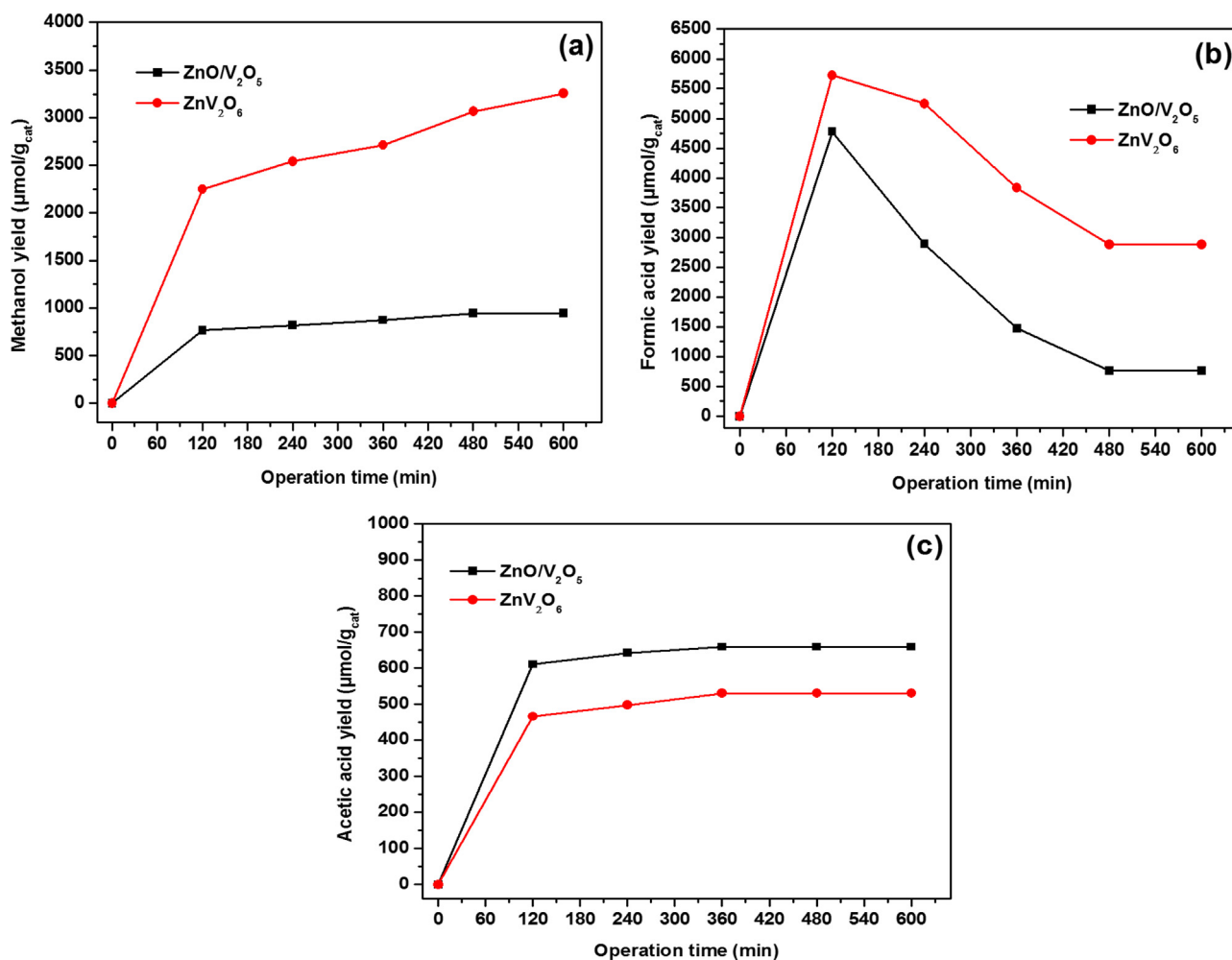**Fig. 8.** Effect of irradiation time for ZnO/V_2O_5 and ZnV_2O_6 catalyst for CO_2 photo-reduction with H_2O: (a) methanol evolution; (b) formic acid evolution; (c) acetic acid evolution.

enhanced photoactivity and selectivity of ZnV_2O_6 nanosheets can be attributed to more production of electrons-hole pairs under visible light irradiations and their improved charges separation in the presence of V_2O_5.

Fig. 8(b) presents a dynamic HCOOH production over ZnO/V_2O_5 and ZnV_2O_6 catalysts at different irradiation time. HCOOH formation over ZnO/V_2O_5 and ZnV_2O_6 presents different behaviour, initially reaching maximum concentration, and then gradually decreased till reached to steady sate. The decreased in HCOOH production over the irradiation time was probably, initially, some amount of CH_3OH was converted to HCOOH, when there was more production of electrons at the start of the reaction [44]. In general, significantly enhanced photoactivity of ZnV_2O_6 nanosheets toward CO_2 reduction was evidently due to uniform growth of ZnV_2O_6 nanosheets using solvothermal method and the exceptional morphological structure associated with ZnV_2O_6. On the other hand, initially the yield of CH_3COOH production is increased and then remained constant after 6 h of irradiation time as depicted in Fig. 8(c). However, the amount of CH_3COOH over ZnO/V_2O_5 catalyst was significantly higher than ZnV_2O_6 samples. This confirms that ZnV_2O_6 nanosheets are less favourable for CH_3COOH production but has potential for selective CO_2 reduction with H_2O to CH_3OH.

The yield and selectivity of all the products is summarized in Table 2. The operating parameters employed during photocatalytic CO_2 reduction with H_2O in solar photoreactor are

Table 2
Summary of product yield rates during photocatalytic CO_2 reduction using different catalysts.

Catalysts	Yield (μmol g-cat^{-1})[a]			Selectivity (%)		
	CH_3OH	HCOOH	CH_3COOH	CH_3OH	HCOOH	CH_3COOH
ZnO/V_2O_5	945.28	761.76	658.69	39.96	32.2	27.84
ZnV_2O_6	3253.84	2886.9	530.1	48.78	43.28	7.95

[a] Yield rates calculated at 10 h irradiation basis.

Table 3
Summary of operating parameters employed in solar type reactor.

System	ZnO/V_2O_5	ZnV_2O_6
Volume	100 cm^3	100 cm^3
Catalyst loading	0.1 g ZnO/V_2O_5	0.1 g ZnV_2O_5
Light source	35 W HID Xenon	35 W HID Xenon
Temperature	25 °C	25 °C
Pressure	1 atm	1 atm
Main product	CH_3OH, HCOOH, CH_3COOH	CH_3OH, HCOOH, CH_3COOH
Yield (CH_3OH)[a] (μmol g-cat^{-1})	945.28	3253.84

[a] Yield rates calculated at 10 h irradiation basis.

presented in Table 3. The yield of CH_3OH over ZnV_2O_6 catalysts is 3253.84 μmol g-cat^{-1}, 3.4 fold higher than CH_3OH yield rate over the bare ZnO/V_2O_5. Additionally, HCOOH yield rate over the ZnV_2O_6
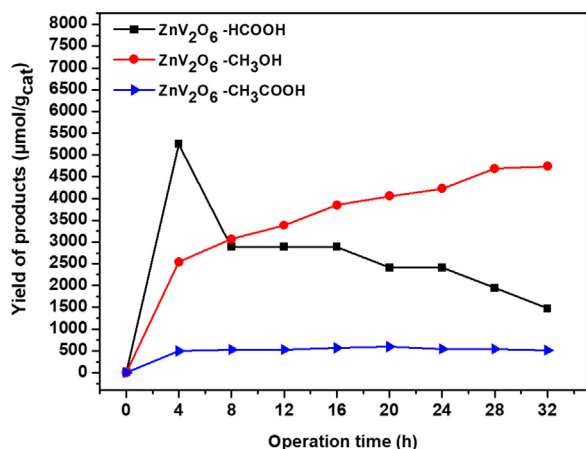
Fig. 9. Stability study under visible light irradiation of ZnV_2O_6 nanosheets catalyst with the following conditions: 100 mg photocatalysts, 100 ml distilled water with 0.1 M NaOH, 35 W HID Xe lamp, room temperature, atmospheric pressure, and feed flow rate 20 ml/min.

Fig. 10. Schematic representation of the reaction mechanism proposed for the photo reduction of CO_2 to CH_3OH, HCOOH and CH_3COOH over ZnV_2O_6 nanosheets under visible light.

higher photoactivity and stability for enhanced CO_2 reduction to solar fuels.

3.3. Mechanism of reaction

ZnV_2O_6 nanosheets is used as photocatalysts to evaluate the photocatalytic activity by photocatalytic reduction of CO_2 into CH_3OH, HCOOH and CH_3COOH. During the reduction process, the major reaction steps were described briefly in Eq. (1) – (7).

$$ZnV_2O_6 + h\nu \rightarrow h^+ + e^- \tag{1}$$

$$V^{3+} + e^- \rightarrow V^{2+} \tag{2}$$

$$H_2O + h^+ \rightarrow {}^\bullet OH + H^+ \tag{3}$$

$$CO_2 + e^- \rightarrow CO_2^\bullet \tag{4}$$

$$CO_2 + 2H^+ + 2e^- \rightarrow HCOOH \tag{5}$$

$$CO_2 + 6H^+ + 6e^- \rightarrow CH_3OH + H_2O \tag{6}$$

$$2CO_2 + 8H^+ + 8e^- \rightarrow CH_3COOH + 2H_2O \tag{7}$$

The production of photo-excited electron-hole pairs is presented in Eq. 1. The presence of V_2O_5 leads to an increase in lifetime of charges and fosters redox reaction at the surfaces (Eq. 2). Reduction of CO_2 occurs at the CB by the electrons while H_2O is oxidized by holes at the VB and this is explained in Eqs. (3) and (4). Production of HCOOH, CH_3OH and CH_3COOH through the reduction of CO_2 by 2, 6 and 8 electrons is discussed in Eqs. (4)–(6). Based on the photoactivity and reaction pathway, insights for the reaction mechanism were obtained.

The schematic representation of the reaction mechanism is depicted in Fig. 10. Under visible light irradiation, the excited electrons moved from the valence band (VB) of ZnV_2O_6 nanosheets to its conduction band (CB). Holes in the valence band of ZnV_2O_6 react with water producing O_2 and H^+. Absorbed CO_2 molecules are reduced to CH_3OH, HCOOH and CH_3COOH by enriched electrons on the ZnV_2O_6 surface. In the case of CO_2 reduction with H_2O, CH_3OH was detected as main product over ZnV_2O_6, probably due to appropriate reduction potential of CO_2/CH_3OH (-0.38 V), than CO_2/CH_3COOH (-0.24 V) and $CO_2/HCOOH$ (-0.61 V), when compared with CB of ZnV_2O_6. Since the reduction potential of CO_2/CH_3OH (-0.38 V) is less than the conduction band of ZnV_2O_6, the reaction was more favourable for its production. However, CH_3COOH needed more electrons and its conduction band much lower than the methanol. On the other hand, formic acid reduction potential is much closer if compared with ZnV_2O_6. The appropriate band alignment of ZnV_2O_6 could help for selective CH_3OH production during CO_2 reduction under visible light irradiation.

is 2886.9 μmol g-cat^{-1}, 3.8 times higher than HCOOH yield rate over ZnO/V_2O_5. On the other hand, the amount of CH_3COOH produced over ZnV_2O_6 was much lower than its yield over ZnO/V_2O_5 catalysts. Therefore, ZnV_2O_6 catalyst is efficient for the production of CH_3OH and HCOOH. The observed selectivity was 49% and 43%, for CH_3OH and HCOOH, respectively. In addition, a small amount of CH_3COOH is produced over ZnV_2O_6. Significantly higher and selective CH_3OH production over ZnV_2O_6 reveals efficient production of electrons and their utilizations during photocatalytic CO_2 reduction process over 2D ZnV_2O_6 nanosheets.

The performance of ZnV_2O_6 nanosheets was further compared with the results reported by previous researchers as depicted in Table 4. CO_2 was converted to CH_3OH using zinc oxide modified reduced graphene oxide nanocomposites (ZnO-rGO) and a yield of 263.1 μmol/g was obtained after 3 h reaction time [45]. Hexamolybdenum cluster compounds (GO-(TBA)$_2$Mo$_6$Br$^i_8$Br^{a}x and GO-Cs$_2$Mo$_6$Br$^i_8$Br^{a}x) were used for CO_2 photo reduction with maximum CH_3OH yield of 1294 and 1644 μmol/g after 24 h, respectively [46]. Lamellar $BiVO_4$ were used for CO_2 photo reduction, a maximum CH_3OH yield of 35 μmol/g was recorded after 6 h reaction [47]. ZnS was used to convert CO_2 to CH_3OH and Chang et al. [48] reported optimum yield of 850 μmol/g after 1 h. The superior yield of CH_3OH obtained in the present study using ZnV_2O_6 2D nanosheets can be attributed to the hierarchical structure with improved charges separation by V_2O_5 and visible light absorption property of ZnV_2O_6 as a result of its suitable band gap.

In order to check the stability of the ZnV_2O_6 nanosheets, a photo-stability test was performed with a cumulative 32 h irradiation time. The effects of different irradiation times on the activity of ZnV_2O_6 for photocatalytic CO_2 reduction to CH_3OH, HCOOH and CH_3COOH at room temperature, atmospheric pressure, and feed flow rate 20 ml/min are presented in Fig. 9. Evidently, CH_3OH and CH_3COOH concentrations gradually increased until reached to steady state in the entire irradiation period, while the yield of HCOOH was decreased significantly. At the start of the reaction, the photocatalytic CO_2 reduction into HCOOH was significantly higher in ZnV_2O_6 catalyst, possibly due to initially some amount of CH_3OH was converted to HCOOH, when there was more production of electrons. The maximum HCOOH production was observed initially and then gradually reduced over the irradiation time. Using ZnV_2O_6 nanosheets, CH_3OH was observed as the main product during CO_2 photo-reduction. More importantly, catalyst prevailed sustainability even after 32 h of irradiation for continuous production of CH_3OH. Therefore, novel ZnV_2O_6 nanosheets provides
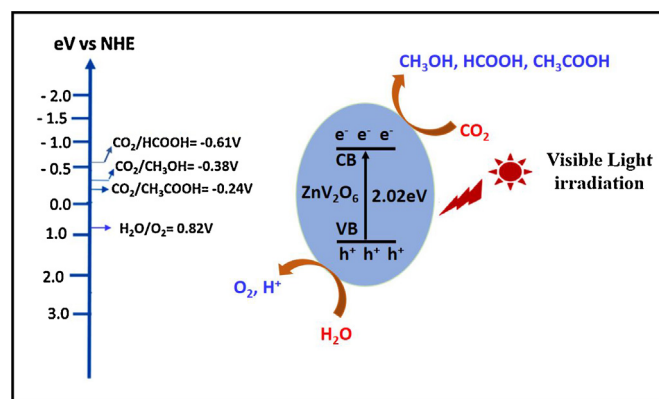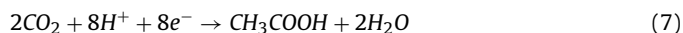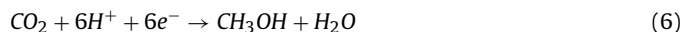
Table 4
Summary of products yield rates during photocatalytic CO_2 reduction using different catalysts.

Catalysts	Yield (μmol g-cat^{-1})			Light Source	Catalyst Used	Ref.
	CH_3OH	HCOOH	CH_3COOH			
ZnO/V_2O_5	945.28	761.76	658.69	35 W HID Xe lamp, 20 MW cm^{-2}	0.1 g	Current Study
ZnV_2O_6	3253.84	2886.9	530.1	35 W HID Xe lamp, 20 MW cm^{-2}	0.1 g	Current Study
ZnO-rGO	263.1	–	–	300 W Xenon lamp	0.1 g	[45]
GO-(TBA)$_2$Mo$_6$Br$^i_8$Br^{a}x	1294	–	–	20 W visible light (75 W m^{-2})	0.1 g	[46]
GO- Cs$_2$Mo$_6$Br$^i_8$Br^{a}x	1644	–	–	20 W visible light (75 W m^{-2})	0.1 g	[46]
$BiVO_4$	35	–	–	300 W Xe-lamp	0.2 g	[47]
ZnS	850	–	–	Monochromatic 355-nm pulsed laser radiations	0.1 g	[48]
Ag-g-C$_3$N$_4$/WO$_3$	1750	–	–	LED; Epitex, 30M32L	0.003 g	[49]
Au/Ag-g-C$_3$N$_4$/WO$_3$	2500	–	–	LED; Epitex, 30M32L	0.003 g	[49]

Therefore, production of CH_3OH was significantly enhanced using novel ZnV_2O_6 nanosheets because of efficient visible light absorption, appropriate band structure and higher electron mobility with hindered recombination rate by V_2O_5.

4. Conclusions

In this work, ZnV_2O_6 hierarchical nanosheets were successfully prepared by one-step solvothermal method for photocatalytic CO_2 reduction with H_2O in a solar photoreactor. By coupling of vanadium with ZnO shifted band gap energy towards visible region and the pure ZnV_2O_6 nanosheets were produced with hierarchical structure. The hierarchical ZnV_2O_6 nanosheets showed enhanced photocatalytic activity and hindered charges recombination rate for photocatalytic CO_2 reduction with H_2O to CH_3OH, HCOOH and CH_3COOH. Hierarchical ZnV_2O_6 nanosheets favoured CH_3OH production with highest efficiency and better stability. Yield rate of CH_3OH as the main product over ZnV_2O_6 catalyst was 3253.84 μmol g-cat^{-1} under visible light irradiation. The enhanced photocatalytic activity and stability over ZnV_2O_6 structure can be attributed to hierarchical structure with enhanced charge separation. This work indicates that hierarchical ternary materials could be used as a promising photo-catalyst for the photo-reduction of CO_2 to solar fuels.

Acknowledgement

References

[1] A. Meng, B. Zhu, B. Zhong, L. Zhang, B. Cheng, Direct Z-scheme TiO$_2$/CdS hierarchical photocatalyst for enhanced photocatalytic H$_2$-production activity, Appl. Surf. Sci. 422 (2017) 518–527.

[2] B. Tahir, M. Tahir, N.S. Amin, Gold–indium modified TiO$_2$ nanocatalysts for photocatalytic CO$_2$ reduction with H$_2$ as reductant in a monolith photoreactor, Appl. Surf. Sci. 338 (2015) 1–14.

[3] M. Tahir, Synergistic effect in MMT-dispersed Au/TiO$_2$ monolithic nanocatalyst for plasmon-absorption and metallic interband transitions dynamic CO$_2$ photo-reduction to CO, Appl. Catal. B: Environ. 219 (2017) 329–343.

[4] J. Mao, K. Li, T. Peng, Recent advances in the photocatalytic CO$_2$ reduction over semiconductors, Catal. Sci. Technol. 3 (2013) 2481–2498.

[5] J. Yu, J. Jin, B. Cheng, M. Jaroniec, A noble metal-free reduced graphene oxide–CdS nanorod composite for the enhanced visible-light photocatalytic reduction of CO$_2$ to solar fuel, J. Mater. Chem. A 2 (2014) 3407–3416.

[6] D.-S. Lee, H.-J. Chen, Y.-W. Chen, Photocatalytic reduction of carbon dioxide with water using InNbO$_4$ catalyst with NiO and Co$_3$O$_4$ cocatalysts, J. Phys. Chem. Solids 73 (2012) 661–669.

[7] B. Tahir, M. Tahir, N.A.S. Amin, Photo-induced CO$_2$ reduction by CH$_4$/H$_2$O to fuels over Cu-modified g-C$_3$N$_4$ nanorods under simulated solar energy, Appl. Surf. Sci. 419 (2017) 875–885.

[8] Y. Matsumoto, M. Obata, J. Hombo, Photocatalytic reduction of carbon dioxide on p-type CaFe$_2$O$_4$ powder, J. Phys. Chem. 98 (1994) 2950–2951.

[9] J. Low, B. Cheng, J. Yu, Surface modification and enhanced photocatalytic CO$_2$ reduction performance of TiO$_2$: a review, Appl. Surf. Sci. 392 (2017) 658–686.

[10] M. Tahir, B. Tahir, Dynamic photocatalytic reduction of CO$_2$ to CO in a honeycomb monolith reactor loaded with Cu and N doped TiO$_2$ nanocatalysts, Appl. Surf. Sci. 377 (2016) 244–252.

[11] E. Liu, L. Kang, F. Wu, T. Sun, X. Hu, Y. Yang, H. Liu, J. Fan, Photocatalytic reduction of CO$_2$ into methanol over Ag/TiO$_2$ nanocomposites enhanced by surface plasmon resonance, Plasmonics 9 (2014) 61–70.

[12] N. Matinise, X. Fuku, K. Kaviyarasu, N. Mayedwa, M. Maaza, ZnO nanoparticles via *Moringa oleifera* green synthesis: physical properties & mechanism of formation, Appl. Surf. Sci. 406 (2017) 339–347.

[13] A. Yahaya, M. Gondal, A. Hameed, Selective laser enhanced photocatalytic conversion of CO$_2$ into methanol, Chem. Phys. Lett. 400 (2004) 206–212.

[14] G. Mahmodi, S. Sharifnia, F. Rahimpour, S. Hosseini, Photocatalytic conversion of CO$_2$ and CH$_4$ using ZnO coated mesh: effect of operational parameters and optimization, Sol. Energy Mater. Sol. Cells 111 (2013) 31–40.

[15] I.A. Mkhalid, Preparation and characterization of NaBiO$_3$ nanopowders by different methods for photocatalytic reduction of CO$_2$, Ceram. Int. 40 (2014) 5795–5800.

[16] V.S. Kosera, T.M. Cruz, E.S. Chaves, E.R. Tiburtius, Triclosan degradation by heterogeneous photocatalysis using ZnO immobilized in biopolymer as catalyst, J. Photochem. Photobiol. A: Chem. 344 (2017) 184–191.

[17] N. Daneshvar, D. Salari, A. Khataee, Photocatalytic degradation of azo dye acid red 14 in water on ZnO as an alternative catalyst to TiO$_2$, J. Photochem. Photobiol. A: Chem. 162 (2004) 317–322.

[18] S.G. Kumar, K.S.R.K. Rao, Zinc oxide based photocatalysis: tailoring surface-bulk structure and related interfacial charge carrier dynamics for better environmental applications, RSC Adv. 5 (2015) 3306–3351.

[19] L. Vayssieres, Growth of arrayed nanorods and nanowires of ZnO from aqueous solutions, Adv. Mater. 15 (2003) 464–466.

[20] C. Tian, Q. Zhang, A. Wu, M. Jiang, Z. Liang, B. Jiang, H. Fu, Cost-effective large-scale synthesis of ZnO photocatalyst with excellent performance for dye photodegradation, Chem. Commun. 48 (2012) 2858–2860.

[21] R. Khan, M.S. Hassan, L.-W. Jang, J. Hyeon Yun, H.-K. Ahn, M.-S. Khil, I.-H. Lee, Low-temperature synthesis of ZnO quantum dots for photocatalytic degradation of methyl orange dye under UV irradiation, Ceram. Int. 40 (2014) 14827–14831.

[22] C. Yu, K. Yang, Y. Xie, Q. Fan, J.C. Yu, Q. Shu, C. Wang, Novel hollow Pt-ZnO nanocomposite microspheres with hierarchical structure and enhanced photocatalytic activity and stability, Nanoscale 5 (2013) 2142–2151.

[23] M. Pirhashemi, A. Habibi-Yangjeh, Preparation of novel nanocomposites by deposition of Ag$_2$WO$_4$ and AgI over ZnO particles: efficient plasmonic visible-light-driven photocatalysts through a cascade mechanism, Ceram. Int. 43 (2017) 13447–13460.

[24] A. Yarahmadi, S. Sharifnia, Dye photosensitization of ZnO with metallophthalocyanines (Co, Ni and Cu) in photocatalytic conversion of greenhouse gases, Dyes Pigm. 107 (2014) 140–145.

[25] C. Chen, T. Liu, L. Lin, X. Xie, X. Chen, Q. Liu, B. Liang, W. Yu, C. Qiu, Multi-walled carbon nanotube-supported metal-doped ZnO nanoparticles and their photocatalytic property, J. Nanopart. Res. 15 (2013) 1295.

[26] X. Li, Q. Wang, Y. Zhao, W. Wu, J. Chen, H. Meng, Green synthesis and photo-catalytic performances for ZnO-reduced graphene oxide nanocomposites, J. Colloid Interface Sci. 411 (2013) 69–75.

[27] S.G. Kumar, K.K. Rao, Comparison of modification strategies towards enhanced charge carrier separation and photocatalytic degradation activity of metal oxide semiconductors (TiO$_2$, WO$_3$ and ZnO), Appl. Surf. Sci. 391 (2017) 124–148.

[28] R. Akbarzadeh, S.B. Umbarkar, R.S. Sonawane, S. Takle, M.K. Dongare, Vanadia–titania thin films for photocatalytic degradation of formaldehyde in sunlight, Appl. Catal. A: Gen. 374 (2010) 103–109.

[29] J. Su, X.-X. Zou, G.-D. Li, X. Wei, C. Yan, Y.-N. Wang, J. Zhao, L.-J. Zhou, J.-S. Chen, Macroporous V$_2$O$_5$–BiVO$_4$ composites: effect of heterojunction on the behavior of photogenerated charges, J. Phys. Chem. C 115 (2011) 8064–8071.

[30] J. Zhu, L. Cao, Y. Wu, Y. Gong, Z. Liu, H.E. Hoster, Y. Zhang, S. Zhang, S. Yang, Q. Yan, Building 3D structures of vanadium pentoxide nanosheets and application as electrodes in supercapacitors, Nano Lett. 13 (2013) 5408–5413.

[31] F.K. Butt, M. Tahir, C. Cao, F. Idrees, R. Ahmed, W.S. Khan, Z. Ali, N. Mahmood, M. Tanveer, A. Mahmood, Synthesis of novel ZnV$_2$O$_4$ hierarchical nanospheres

and their applications as electrochemical supercapacitor and hydrogen storage material, ACS Appl. Mater. Interfaces 6 (2014) 13635–13641.

[32] Y. Shi, C. Zhu, L. Wang, C. Zhao, W. Li, K.K. Fung, T. Ma, A. Hagfeldt, N. Wang, Ultrarapid sonochemical synthesis of ZnO hierarchical structures: from fundamental research to high efficiencies up to 6.42% for quasi-solid dye-sensitized solar cells, Chem. Mater. 25 (2013) 1000–1012.

[33] F.K. Butt, C. Cao, Q. Wan, P. Li, F. Idrees, M. Tahir, W.S. Khan, Z. Ali, M.J. Zapata, M. Safdar, Synthesis, evolution and hydrogen storage properties of ZnV_2O_4 glomerulus nano/microspheres: a prospective material for energy storage, Int. J. Hydrogen Energy 39 (2014) 7842–7851.

[34] L. Xiao, Y. Zhao, J. Yin, L. Zhang, Clewlike ZnV_2O_4 hollow spheres: nonaqueous sol–gel synthesis, formation mechanism, and lithium storage properties, Chem. Eur. J. 15 (2009) 9442–9450.

[35] F.K. Butt, C. Cao, R. Ahmed, W.S. Khan, T. Cao, N. Bidin, P. Li, Q. Wan, X. Qu, M. Tahir, Synthesis of novel ZnV_2O_4 spinel oxide nanosheets and their hydrogen storage properties, CrystEngComm 16 (2014) 894–899.

[36] F. Duan, W. Dong, D. Shi, M. Chen, Template-free synthesis of ZnV_2O_4 hollow spheres and their application for organic dye removal, Appl. Surf. Sci. 258 (2011) 189–195.

[37] M. Tahir, B. Tahir, N.A.S. Amin, Synergistic effect in plasmonic Au/Ag alloy NPs co-coated TiO_2 NWs toward visible-light enhanced CO_2 photoreduction to fuels, Appl. Catal. B: Environ. 204 (2017) 548–560.

[38] Z. Yin, J. Qin, W. Wang, M. Cao, Rationally designed hollow precursor-derived $Zn_3V_2O_8$ nanocages as a high-performance anode material for lithium-ion batteries, Nano Energy 31 (2017) 367–376.

[39] T. Zhang, Y. Shen, Y.-H. Qiu, Y. Liu, R. Xiong, J. Shi, J. Wei, Facial synthesis and photoreaction mechanism of $BiFeO_3/Bi_2Fe_4O_9$ heterojunction nanofibers, ACS Sustain. Chem. Eng. 5 (5) (2017) 2142–2151.

[40] H.A. Almukhlifi, R.C. Burns, Oxidative dehydrogenation of isobutane to isobutene by pyrovanadates, $M_2V_2O_7$, where M (II) = Mn, Co, Ni, Cu and Zn, and Co_2VO_4 and ZnV_2O_4: The effect of gold nanoparticles, J. Mol. Catal. A: Chem. 408 (2015) 26–40.

[41] H. Liu, W. Yang, Ultralong single crystalline V_2O_5 nanowire/graphene composite fabricated by a facile green approach and its lithium storage behavior, Energy Environ. Sci. 4 (2011) 4000–4008.

[42] M. Aslam, I.M. Ismail, T. Almeelbi, N. Salah, S. Chandrasekaran, A. Hameed, Enhanced photocatalytic activity of V_2O_5–ZnO composites for the mineralization of nitrophenols, Chemosphere 117 (2014) 115–123.

[43] S.-m. Chang, W.-s. Liu, Surface doping is more beneficial than bulk doping to the photocatalytic activity of vanadium-doped TiO_2, Appl. Catal. B: Environ. 101 (2011) 333–342.

[44] M. Tahir, B. Tahir, N.A.S. Amin, Z.Y. Zakaria, Photo-induced reduction of CO_2 to CO with hydrogen over plasmonic Ag-NPs/TiO_2 NWs core/shell hetero-junction under UV and visible light, J. CO_2 Util. 18 (2017) 250–260.

[45] L. Zhang, N. Li, H. Jiu, G. Qi, Y. Huang, ZnO-reduced graphene oxide nanocomposites as efficient photocatalysts for photocatalytic reduction of CO_2, Ceram. Int. 41 (2015) 6256–6262.

[46] P. Kumar, H.P. Mungse, S. Cordier, R. Boukherroub, O.P. Khatri, S.L. Jain, Hexamolybdenum clusters supported on graphene oxide: visible-light induced photocatalytic reduction of carbon dioxide into methanol, Carbon 94 (2015) 91–100.

[47] J. Mao, T. Peng, X. Zhang, K. Li, L. Zan, Selective methanol production from photocatalytic reduction of CO_2 on $BiVO_4$ under visible light irradiation, Catal. Commun. 28 (2012) 38–41.

[48] X. Chang, J. Zheng, M. Gondal, G. Ji, Photocatalytic conversion of CO_2 into value-added hydrocarbon (methanol) with high selectivity over ZnS nanoparticles driven by 355-nm pulsed laser, Res. Chem. Intermed. 41 (2015) 739–747.

[49] T. Ohno, N. Murakami, T. Koyanagi, Y. Yang, Photocatalytic reduction of CO_2 over a hybrid photocatalyst composed of WO_3 and graphitic carbon nitride (gC_3N_4) under visible light, J. CO_2 Util. 6 (2014) 17–25.